Ge et al. *Light: Science & Applications* (2026)15:73
https://doi.org/10.1038/s41377-025-02127-y

ARTICLE **Open Access**

A near-infrared Sn-Pb perovskite imager with monolithic integration

Ciyu Ge[1], Chengjie Deng[1,2], Jiaxing Zhu[1], Yongcheng Zhu[1], Qi Xu[1], Borui Jiang[1], Long Chen[1,3], Yuxuan Liu[4], Boxiang Song[1,3,5], Ping Fu[6], Chao Chen[1,3]✉, Liang Gao[1,2,3,4,7]✉ and Jiang Tang[1,3]✉

Abstract

Solution-processed Sn-Pb perovskites have emerged as promising candidates for near-infrared (NIR) photodetectors due to their low-cost, tunable bandgap and scalable fabrication. However, Sn^{2+} oxidation creates Sn vacancies and undesirable p-type doping, resulting in high dark current and limited detectivity, which hinder the practical deployment of Sn-Pb perovskite photodetectors. Herein, we propose a $Sn(SCN)_2$ inorganic molecular surface passivation strategy to suppress Sn^{2+} oxidation, significantly reduce surface defect density and enhance the optoelectronic properties (a dark current density of 10 nA cm^{-2} at a bias of −0.1 V and a high specific detectivity of ~1.6×10^{13} Jones). Leveraging this approach, we report the monolithically integrated Sn-Pb perovskite NIR imager with a complementary metal-oxide-semiconductor readout circuit. The imager, featuring a 640 × 512 pixel array with a 15 µm pixel pitch, achieves an external quantum efficiency of 76% at 940 nm and a modulation transfer function of 206.5 LW/PH at 50%. Furthermore, the Sn-Pb perovskite imager demonstrates advanced material recognition capabilities, including liquid identification, underscoring its potential in chemical sensing, biomedical imaging and industrial inspection.

Introduction

Photodetectors, which convert incident light signals into modulated electrical signals, are critical components in modern optoelectronics[1–5]. Particularly, near-infrared (NIR) photodetectors afford for widespread applications in security screening[6,7], material identification[8], machine vision[9,10] and autonomous driving[11,12]. Recently, emerging photodetectors based on organic semiconductors and quantum dots have gained significant attention due to their tunable bandgaps and low-temperature solution-processability. However, the external quantum efficiency (EQE) in the NIR region remain significantly lower than in the visible spectrum (typically below 60%)[13–15].

Halide perovskites, with high absorption coefficient, high carrier mobility, low production cost and compatibility with solution processing, have been widely explored for photovoltaics[16,17], displays[18–24] and photodetection[25–27] applications. Replacing part of Pb in Pb-based perovskites with Sn has been adopted to extend the absorption cut-off edge to ~1000 nm, making Sn-Pb perovskites as promising candidates for NIR photodetectors[28,29]. However, the development of Sn-Pb perovskite-based photodetectors has been limited by the high dark current density and low specific detectivity (D^*)[30–35]. Though the low-temperature solution processing enables monolithic integration with silicon-based readout integrated circuit (ROIC) to form NIR imager, there is still no publicly reported NIR imager based on Sn-Pb perovskite up to now. Indeed, the integration of perovskite with ROIC has been successfully applied to both visible and X-ray imagers[36–39].

One of the main challenges is the delocalized $5s^2$ lone pair electrons of Sn^{2+} make it susceptible to be oxidized into Sn^{4+}, leading to the detrimental Sn vacancies (V_{Sn}) and undesirable p-type doping[40–42]. Many studies have introduced antioxidants or strong complexing agents (e.g., SnF_2[43], Sn powder[44], tin acetate ($Sn(Ac)_2$[45])) into Sn-Pb perovskite precursors to mitigate bulk oxidation.

Correspondence: Chao Chen (cchen@hust.edu.cn) or
Liang Gao (highlight@hust.edu.cn) or Jiang Tang (jtang@mail.hust.edu.cn)
[1] Wuhan National Laboratory for Optoelectronics (WNLO) and School of Optical and Electronic Information (SOEI), Huazhong University of Science and Technology, Wuhan, China
[2] State Key Laboratory of Pulsed Power Laser Technology, Hefei, China
Full list of author information is available at the end of the article

© The Author(s) 2026

Open Access This article is licensed under a Creative Commons Attribution 4.0 International License, which permits use, sharing, adaptation, distribution and reproduction in any medium or format, as long as you give appropriate credit to the original author(s) and the source, provide a link to the Creative Commons licence, and indicate if changes were made. The images or other third party material in this article are included in the article's Creative Commons licence, unless indicated otherwise in a credit line to the material. If material is not included in the article's Creative Commons licence and your intended use is not permitted by statutory regulation or exceeds the permitted use, you will need to obtain permission directly from the copyright holder. To view a copy of this licence, visit http://creativecommons.org/licenses/by/4.0/.

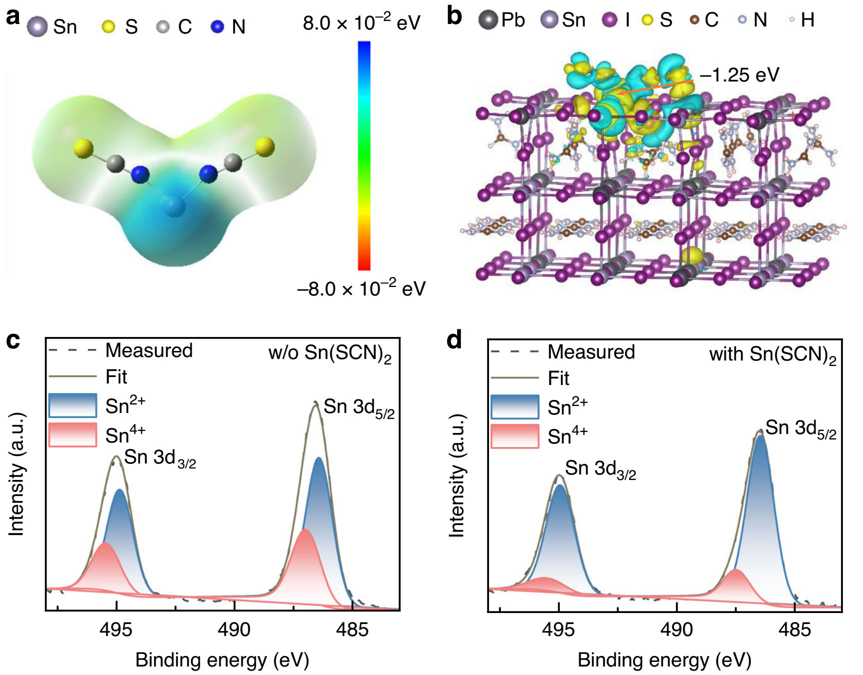

Fig. 1 Material properties and interconnection mechanism between Sn(SCN)$_2$ and perovskite. **a** Structure and ESP of Sn(SCN)$_2$. **b** Atomic structure and adsorption energy of Sn(SCN)$_2$ absorbed on the perovskite surface. **c**, **d** Sn 3 d XPS spectra of Sn-Pb perovskite films

Choy et al., introduced Sn(SCN)$_2$ into the Sn-Pb perovskite precursor, utilizing the pseudo-halide SCN$^-$ to regulate the crystallization processes and improve the performance of NIR photodetectors[46]. However, the surface of Sn-Pb perovskites remains prone to oxidation during subsequent device fabrication and operation. Consequently, the defect state density at the upper interface of Sn-Pb perovskites is three orders of magnitude higher than that in the bulk[47,48]. Although some studies have successfully suppressed the dark current density by optimizing the electron transport layer, this often comes at the cost of reduced responsivity and EQE, leading to a lower D^*[49]. Suppressing surface oxidation and reducing interface defect density are key to simultaneously minimizing dark current density and enhancing the detectivity of Sn-Pb perovskite photodetectors and imagers.

In this work, we propose a surface passivation strategy using Sn(SCN)$_2$ molecular crystals to address these challenges. Density functional theory (DFT) calculations reveal that the Sn^{2+} in Sn(SCN)$_2$ preferentially interact with V_{Sn} on the perovskite surface and is adsorbed via coordination bonding, effectively passivating the surface defects. The resulting Sn-Pb perovskite photodetectors exhibit an ultralow dark current density (10 nA cm^{-2} at −0.1 V) and a high D^* (~1.6 × 10^{13} Jones). We firstly report a NIR imager that monolithically integrates Sn-Pb perovskite with a larger-scale ROIC made using complementary metal–oxide–semiconductor (CMOS) around the world. The imager are integrated with a CMOS ROIC of 640 × 512 pixel array (15 µm pixel pitch) shows an EQE of 76% at 940 nm and an MTF50 (modulation transfer function at 50% contrast) of 206.5 LW/PH. Our imager demonstrates the liquid identification capabilities, showing it can be used for matter identification.

Results

Interfacial passivation mechanisms on Sn-Pb perovskite film

We designed and synthesized Sn(SCN)$_2$ molecules[50] (supplementary Note 1, Fig. S1, S2) to effectively passivate V_{Sn} in Sn-Pb perovskite interface. We analyzed the charge distribution of Sn(SCN)$_2$ using molecular electrostatic potential (ESP) mapping (Fig. 1a), identifying the Sn^{2+} ions in Sn(SCN)$_2$ as potential interaction sites with the surface of Sn-Pb perovskites. Furthermore, we calculated the adsorption energy of Sn(SCN)$_2$ molecules on the Sn-Pb perovskite surface (Fig. 1b), obtaining a value of −1.25 eV. Fourier transform infrared (FTIR) spectra reveal C = N stretching peak shifts from 1712.30 cm^{-1} to 1711.67 cm^{-1} after Sn(SCN)$_2$ passivation (Fig. S3), indicating an interaction between Sn(SCN)$_2$ and the perovskite surface. These results demonstrate that Sn(SCN)$_2$ can adsorb onto the Sn-Pb perovskite surface via coordination bonding, filling V_{Sn} and mitigating surface defects.

Additionally, $Sn(SCN)_2$, as a molecular crystal, features significant steric hindrance between adjacent Sn^{2+} ions, making the formation of $Sn(SCN)_4$ or other Sn^{4+}-based oxidation products unlikely. This property is critical for suppressing the oxidation of Sn^{2+} on the surface of Sn-Pb perovskites. The Sn 3 d X-ray photoelectron spectroscopy (XPS) spectra of the Sn-Pb perovskite films (Fig. 1c, d) confirmed that $Sn(SCN)_2$ effectively inhibits the oxidation of Sn^{2+}. Notably, the Sn^{4+} content decreased significantly from 34.71% to 13.01%. Ultraviolet photoelectron spectroscopy (UPS) reveals that $Sn(SCN)_2$ passivation raises the Fermi level of the perovskite film (Fig. S4a). Correspondingly, the near surface electron concentration increases from $1.1 \times 10^{10}\,\mathrm{cm}^{-3}$ to $7.6 \times 10^{10}\,\mathrm{cm}^{-3}$ (Fig. S4b), providing strong evidence for the effective reduction of surface V_{Sn}. Therefore, the use of $Sn(SCN)_2$ not only passivates V_{Sn} on the Sn-Pb perovskite surface but also suppresses the oxidation of surface Sn^{2+}, ultimately reducing the surface defect density.

Improved Sn-Pb perovskite film quality and underlying mechanism

Furthermore, we characterized and analyzed Sn-Pb perovskite films before and after $Sn(SCN)_2$ treatment. Scanning electron microscopy (SEM) images (Fig. 2a, b) revealed that $Sn(SCN)_2$ predominantly accumulates at the grain boundaries of the perovskite film, likely due to its primary role on passivating grain boundary defects. This treatment effectively fills voids at the grain boundaries, reducing the surface roughness from 51.7 nm to 42.8 nm and resulting in a smoother and more uniform film morphology (Fig. 2c, d).

Kelvin probe force microscopy (KPFM) results further confirmed a reduction in the overall surface potential and a more uniform potential distribution (Fig. 2e). The dashed lines in Fig. 2e represent the horizontal surface potential distribution, further detailed in Fig. 2f. After $Sn(SCN)_2$ treatment, the potential difference decreases significantly from 314.66 mV to 224.68 mV, reflecting improved uniformity of the surface potential. These results suggest that $Sn(SCN)_2$ effectively passivates surface defects, indicating a lower work function and reduced p-type self-doping. These findings are consistent with the observed the decreased Sn^{4+} content as shown in Fig. 1d.

Figure 2g, h show the steady-state photoluminescence (PL) spectra and time-resolved photoluminescence (TRPL) decays of the Sn-Pb perovskite films, respectively. After $Sn(SCN)_2$ treatment, the Sn-Pb perovskite film exhibits significantly enhanced PL intensity, and its carrier lifetime increases from 125 ns to 461 ns. Furthermore, we compared the defect distribution in perovskite films via drive-level capacitance profiling (DLCP, Fig. 2i). The results revealed that the defect density in the bulk and at the lower interface of the perovskite films remains nearly unchanged, but the defect density at the upper interface decreases by two orders of magnitude after $Sn(SCN)_2$ treatment. Time-of-flight secondary ion mass spectrometry (ToF-SIMS) analysis provides additional evidence that $Sn(SCN)_2$ mainly interacts with the surface of the Sn-Pb perovskite film (Fig. S5). The findings align well with the PL and TRPL observations, indicating that $Sn(SCN)_2$ treatment effectively suppresses nonradiative recombination at the film surface and reduces surface defects.

Performance of Sn-Pb perovskite photodetector

We fabricated Sn-Pb perovskite photodetectors with the structure of ITO/PEDOT:PSS/Sn-Pb perovskite film/C_{60}/BCP/Ag. After $Sn(SCN)_2$ treatment on the upper interface of the Sn-Pb perovskite film, the dark current density of the photodetector significantly decreases with improved uniformity (Figs. 3a, S6). At a bias of $-0.1\,\mathrm{V}$, the dark current density reduces from $61\,\mathrm{nA\,cm}^{-2}$ to $10\,\mathrm{nA\,cm}^{-2}$, which can be attributed to lower defect state density at the film surface. We also measured the photocurrent density curve under 940 nm monochromatic light with a power density of $500\,\mu\mathrm{W/cm}^2$, and the detector with $Sn(SCN)_2$ exhibited a higher photocurrent density. Under varying light intensities from ~0.3 μW to 90 mW, the photocurrent is linearly proportional to the light intensity. Notably, in the self-powered state (zero bias), the $Sn(SCN)_2$-treated Sn-Pb perovskite photodetector achieves a linear dynamic range (LDR) of 147 dB, comparable to that of silicon photodiodes.

We tested the transient response of the photodetector after $Sn(SCN)_2$ treatment. In the self-powered state, the rising and falling times of the device are 0.48 μs and 0.34 μs, respectively (Fig. 3c). Compared to the photodetector without $Sn(SCN)_2$ treatment (Fig. S7), the device with $Sn(SCN)_2$ exhibits a faster response speed and lower parasitic capacitance during charging and discharging, benefiting from effective passivation of interface defects. Additionally, the frequency response of the device demonstrates a $-3\,\mathrm{dB}$ bandwidth of up to 97.2 kHz (Fig. 3d), echoing the observed transient response. The responsivity slightly increases with the light modulation frequency, attributed to the discharge of junction capacitance. This phenomenon has also been observed in PbS quantum dots, Si/Ge and InGaAs photodiodes[51,52]. This rapid photoresponse is adequate to support typical imaging applications running at 30 frames per second[53].

EQE spectra indicate that the Sn-Pb perovskite photodetector exhibits excellent photoresponse across a broad wavelength range of 300–1000 nm (Fig. 3e). After $Sn(SCN)_2$ treatment, the photodetector achieves a higher EQE of 76% at 940 nm. This improvement is attributed to the reduced defect state density at the perovskite film surface. Additionally, the $Sn(SCN)_2$-treated photodetector

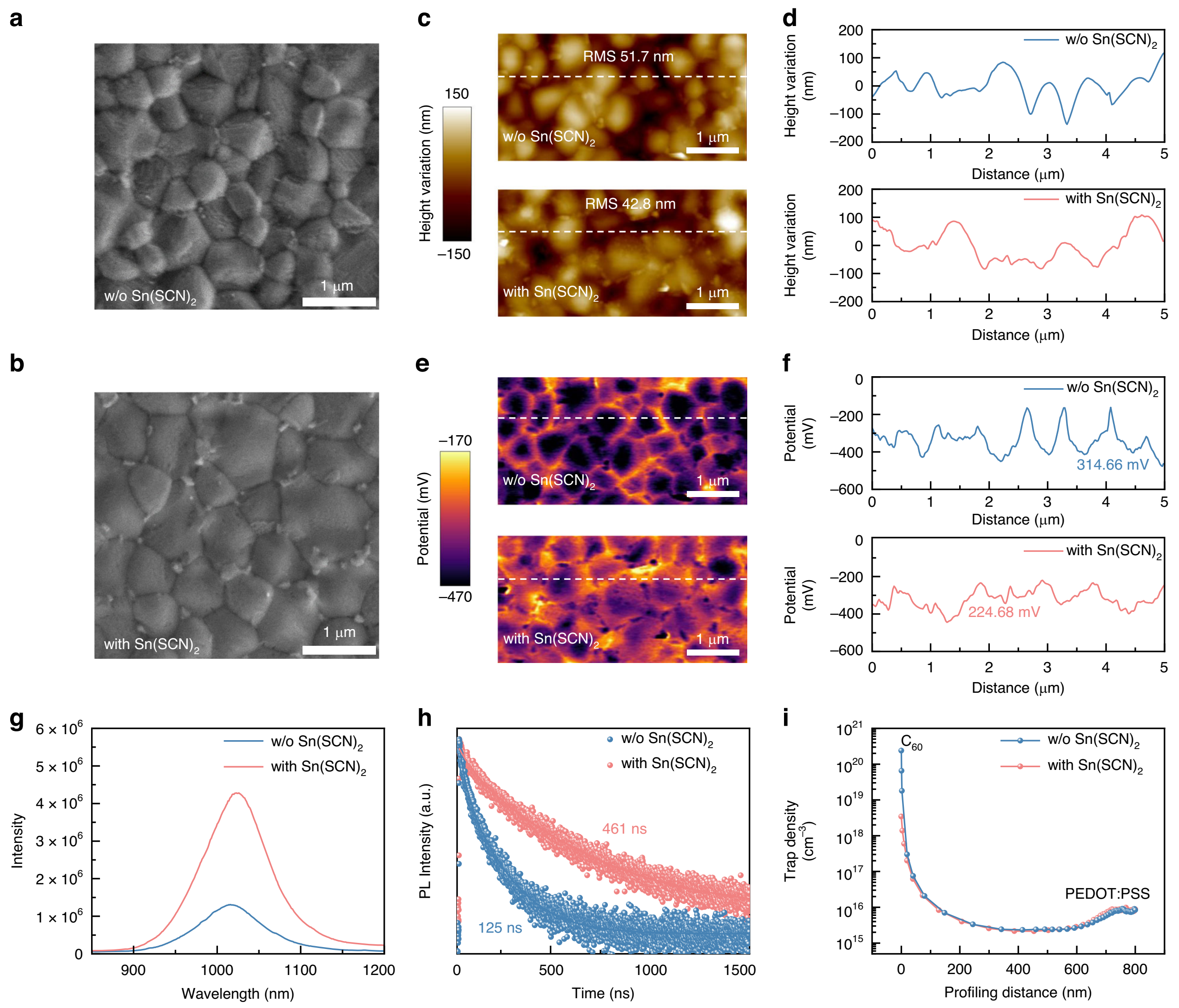

Fig. 2 Passivation of Sn-Pb perovskite film surface with Sn(SCN)$_2$. a, **b** Top-view SEM images of Sn-Pb perovskite films. **c** AFM images of Sn-Pb perovskite films. **d** Profiling surface roughness along the white dash line in (**c**). **e** KPFM images of Sn-Pb perovskite films. **f** Profiling surface potential along the white dash line in (**e**). **g** Steady-state PL spectra of Sn-Pb perovskite films deposited on bare glass. **h** TRPL spectra of Sn-Pb perovskite films deposited on bare glass. **i** DLCP measurements for Sn-Pb perovskite films

demonstrates a higher responsivity (R), achieving 0.58 A/W at 940 nm under a self-powered mode (Fig. 3f).

Figure 3g presents the frequency-dependent current noise spectra at zero bias, directly measured using a preamplifier and lock-in amplifier. Notably, the background noise limit is lower than that of the devices. The photodetector treated with Sn(SCN)$_2$ exhibits a noise current (i_n) an order of magnitude lower than that of the control device, measuring only ~9.76 fA/Hz$^{-1/2}$ at 1 kHz. This substantial reduction in noise current suggests that our approach effectively suppresses $1/f$ noise at high frequency, making it particularly advantageous for imaging applications. We selected the measured noise current at 1 kHz to calculate D^* to ensure consistency with the responsivity measurement conditions. The D^* can be calculated according to the equation,

$$D^* = \frac{R\sqrt{A\Delta f}}{i_n} \tag{1}$$

where A is the device area (0.04 cm^2), Δf is the electrical bandwidth as 1 Hz here. The D^* of Sn(SCN)$_2$-treated Sn-Pb perovskite photodetector achieves ~1.6×10^{13} Jones, which is 13 times higher than the control photodetector (Fig. 3h) and comparable to a commercial InGaAs photodiode[54] (around 4×10^{12} Jones). Among all the reported Sn-Pb perovskite photodiodes, our device simultaneously achieves the highest D^* and the lowest

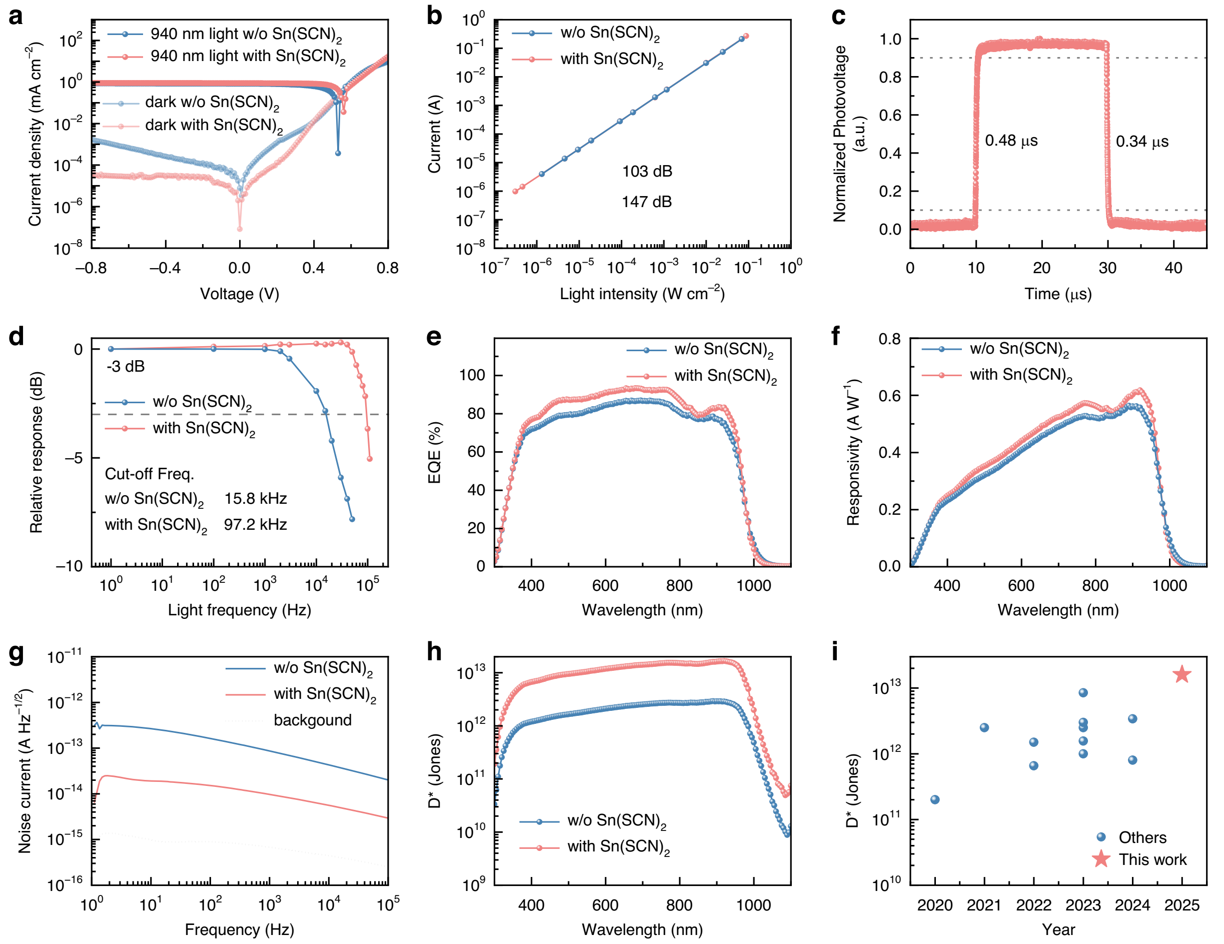

Fig. 3 Performance of CMOS-compatible Sn-Pb perovskite photodetectors. a Current density versus voltage curves of Sn-Pb perovskite photodetectors under dark and 940 nm light with a power density of 500 μW/cm^2. **b** LDR of the Sn-Pb perovskite photodetectors. **c** Transient response of Sn-Pb perovskite photodetectors with $Sn(SCN)_2$ at zero bias. **d** Response bandwidth of Sn-Pb perovskite photodetectors at zero bias. **e** EQE of Sn-Pb perovskite photodetectors. **f** Responsivity spectra of Sn-Pb perovskite photodetectors. **g** Measured noise current of Sn-Pb perovskite photodetectors at zero bias. **h** Detectivity versus wavelength of Sn-Pb perovskite photodetectors. **i** Specific detectivity over 900 nm of Sn-Pb perovskite photodiodes reported in the literatures

dark current density (Fig. 3i). We also measured the EQE, noise current, and D^* at -0.1 V bias (Fig. S8). The results indicate that the variations in these key metrics between 0 V and -0.1 V are minimal. This is because Sn-Pb perovskites exhibit a strong built-in electric field, ensuring that the carrier collection efficiency remains nearly unchanged within this bias voltage range. It is worth noting that the passivation behavior of $Sn(SCN)_2$ differs from our previous report using $Pb(SCN)_2$ additives in the precursor solution. In that case, Pb(SCN) $_2$ could be homogeneously incorporated into the bulk without hindering carrier transport, thereby reducing bulk defect density. We note that incorporating $Sn(SCN)_2$ into the perovskite precursor can also effectively suppress the dark current density (21 nA cm^{-2} at -0.1 V, Fig. S9a). However, due to the intrinsically poor conductivity of $Sn(SCN)_2$, its incorporation into the bulk phase hindered carrier transport, leading to reduced EQE in the resulting Sn-Pb perovskite detector (Fig. S9b), which is detrimental for imaging applications. Therefore, in this work, we focused on employing $Sn(SCN)_2$ as a surface passivation strategy, which simultaneously achieves dark current suppression and maintains high EQE.

Additionally, the device exhibited good operational stability. The dark current density of devices with $Sn(SCN)_2$ exhibited negligible variation after 20 days of storage (Fig. S10a). In contrast, devices without $Sn(SCN)_2$ displayed an increase of nearly two orders of magnitude at -0.1 V (Fig. S10b). For $Sn(SCN)_2$-passivated devices, the dark current density rose to about twice its initial value after storage at 65 °C in nitrogen, in stark contrast to the ~15-fold increase observed in devices without passivation (Fig. S10c, d). Moreover, the devices with $Sn(SCN)_2$ retained stable dark current density after 24 h continuous working a bias of −0.1 V, while the control devices exhibited a fivefold increase (Fig. S11). The unencapsulated device operated continuously in air for over 1300 seconds with almost no photocurrent degradation (Fig. S12). These advancements highlight that $Sn(SCN)_2$ passivation effectively improves both storage and operation stability of unencapsulated devices and lay a solid foundation for the development of high-quality Sn-Pb perovskite imager integrated with CMOS ROIC.

Performance of Sn-Pb perovskite imager

Prior to testing the chip performance, we examined single-pixel devices with different electrode materials (Fig. S13). The measured dark current densities are nearly same, demonstrating that substituting ITO with Au on the PEDOT:PSS side has negligible impact on device performance. We fabricated $Sn(SCN)_2$-treated Sn-Pb perovskite photodetectors layer by layer on a CMOS ROIC. The Sn-Pb perovskite imager with 640 × 512 pixels (15 μm pixel pitch) is schematically illustrated in Fig. 4a, with a photograph of the imager as shown in Fig. 4c. The microscopic image of Sn-Pb perovskite photodiodes covering on the CMOS ROIC chip is shown in Fig. S14a and the cross-section SEM image of the Sn-Pb perovskite imager is shown in Fig. S14b. The imaging system shown in Fig. 4b was built to capture NIR images using the Sn-Pb perovskite imager work at −0.1 V bias. Based on calculations in supplementary Note 2, the photoresponse nonuniformity (PRNU) of the Sn-Pb perovskite imager is 3% (Fig. 4d). To further evaluate the noise performance of the imager, we performed blackbody testing to obtain the statistical distribution of the noise voltage across the entire focal plane (Fig. S15). The results show that the noise follows an approximately Gaussian distribution, which ensures uniform pixel response and good imaging quality. Dead pixels are defined as those with signals below 50% of the average signal, while hot pixels are defined as those with effective noise voltages exceeding twice the mean noise voltage. Due to the superior detection performance of the $Sn(SCN)_2$-treated Sn-Pb perovskite photodetectors, the perovskite imager exhibits an exceptionally low fraction of dead pixels (0.01%) and hot pixels (0.24%), demonstrating its excellent imaging quality (Fig. 4e).

ISO 12233 slanted-edge method was used to measure the spatial resolution. A standard test chart captured by the Sn-Pb perovskite imager under a 940 nm LED is shown in Figs. 4f, S16. The MTF was obtained by resolving the diagonal edges marked in the red rectangles. The MTF50 (50% contrast spatial frequency) value of the slant edge is 206.5 LW/PH (Fig. S17), demonstrating imaging performance comparable to that of the commercial InGaAs imager (Fig. S18). The LDR of the imager is 58.2 dB and the noise equivalent power is 16.4 $fW/\sqrt{Hz}$ (supplementary Note 3). Due to its high LDR, the photograph of the Dynamic range chart-36 with 36 gray levels in Fig. 4g shows all the gray levels are clearly distinguished by the Sn-Pb perovskite imager.

We finally presented an application of this Sn-Pb perovskite imager. The left side of Fig. 4h shows images of three solvents (H_2O, C_2Cl_4 and C_2H_5OH) captured under visible light, and the absorption spectra of the solvents are shown in Fig. S19a. All three appear as colorless and transparent liquids, making them difficult to distinguish under visible light. The right side of Fig. 4h presents NIR images of the same solvents captured by the Sn-Pb perovskite imager under 940 nm illumination. In these images, H_2O appears darkest, C_2H_5OH lighter, and C_2Cl_4 the lightest, enabling clear differentiation between the three solvents (Fig. S19b–d). We included a video demonstration showcasing the imaging performance of our Sn-Pb perovskite NIR imager (Supplementary Video 2). The video clearly illustrates the absence of image lag, confirming that our reset mechanism effectively clears residual charges and ensures real-time imaging capability. We selected 15 frames in 7 s–7.5 s to identify the effect of residual shadow and found no obvious effect between images in each frame (Fig. S20). The imager without $Sn(SCN)_2$ showed a significant decline in imaging quality after 7 days, and deteriorated severely after 14 days. In contrast, the imager with $Sn(SCN)_2$ maintained good imaging performance even after 14 days, demonstrating its enhanced stability (Fig. S21). This imaging capability and material distinction highlight the broad application potential of the Sn-Pb perovskite imager in diverse scenarios.

Discussion

We proposed an interface passivation strategy for Sn-Pb perovskite films by introducing $Sn(SCN)_2$, achieving high D^* (~1.6×10^{13} Jones) and low current density (10 nA cm^{-2} at −0.1 V). Based on this, we developed the high-performance Sn-Pb perovskite imager with 640 × 512 pixels. We demonstrated the potential of these imagers for distinguishing H_2O, C_2Cl_4 and C_2H_5OH, showcasing its versatility and application potential.

Materials and methods

Materials and solvents

The raw materials and solvents were not subjected to any purification. PbI_2 (99.999%), SnI_2 (99.999%), FAI (>99%) and MAI (>99%), were purchased from Advanced Election Technology Co., Ltd. $Pb(SCN)_2$ (99.5%), CsI (99.999%), $EDAI_2$ (99.5%), PEDOT:PSS and C_{60} were purchased from Xi'an Yuri Solar Co., Ltd. SnF_2 (99%), Sn powder (99.999%), N,N-dimethylformamide (DMF, 99.8%, anhydrous), dimethyl sulfoxide (DMSO,

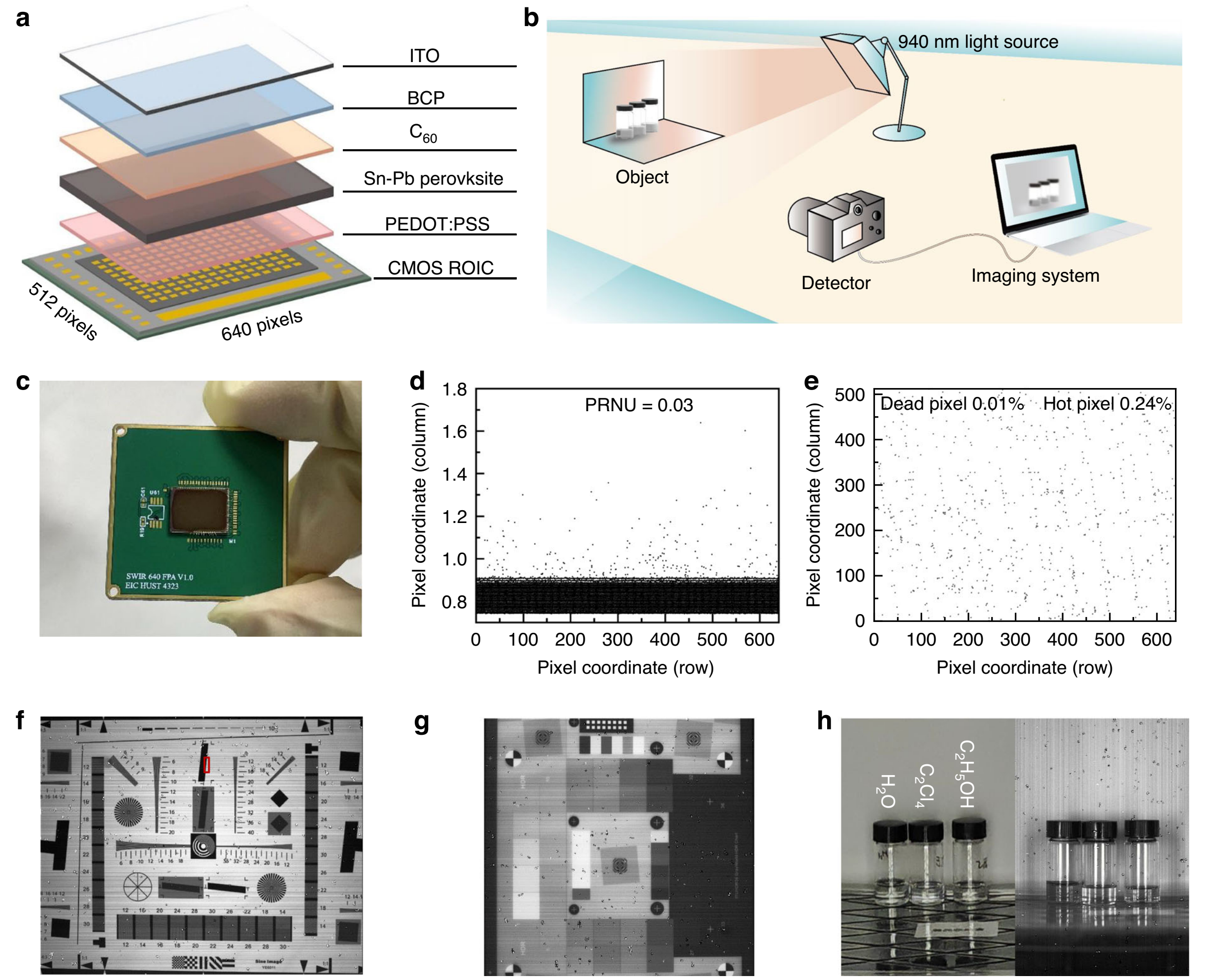

Fig. 4 Performance of Sn-Pb perovskite imager. a Structure diagram of Sn-Pb perovskite imager. **b** Schematic diagram of the imaging processes. **c** Photograph of Sn-Pb perovskite imager. **d** Pixel grayscale distribution of Sn-Pb perovskite imager. **e** Dead pixels and hot pixels of the Sn-Pb perovskite imager. **f** ISO-12233 test chart imaged by the Sn-Pb perovskite imager with a 940 nm LED. **g** Dynamic range chart-36 imaged by the Sn-Pb perovskite imager with a 940 nm LED. **h** Photographs of H_2O, C_2Cl_4 and C_2H_5OH captured by phone camera with a visible light (left) and Sn-Pb perovskite imager with a 940 nm LED (right)

99.9%, anhydrous), chlorobenzene (CB, 99.9%, anhydrous) and isopropanol (IPA, 99.5%, anhydrous) were purchased from Sigma-Aldrich. Bathocuproine (BCP) was purchased from TCI. The glass ITO with a sheet resistance of 7 ~ 9 ohm/sq was purchased from Advanced Election Technology Co. Ltd.

Precursor preparation

The $Cs_{0.1}FA_{0.6}MA_{0.3}Sn_{0.5}Pb_{0.5}I_3$ perovskite precursor with a concentration of 2.0 mol L^{-1} was prepared by mixing CsI (52.0 mg), FAI (206.3 mg), MAI (95.3 mg), SnI_2 (372.6 mg), PbI_2 (461.0 mg), SnF_2 (15.7 mg) and $Pb(SCN)_2$ (3 mg) in mixed solvents of 0.25 mL DMSO and 0.75 mL DMF. The precursor solution was filtered through a 0.22 μm PTFE filter before use.

Theoretical calculation

All calculations in this study were performed with the Vienna ab initio Simulation Package (VASP)[55] within the frame of density functional theory (DFT). The exchange-correlation interactions of electron were described via the generalized gradient approximation (GGA) with PBE functional[56], and the projector augmented wave (PAW) method[57] was used to describe the interactions of electron and ion. Additionally, the DFT-D3 method[58,59] was used to account for the long-range van der Waals forces present within the system. The Monkhorst-Pack scheme[60] was used for the integration in the irreducible Brillouin zone. The kinetic energy cut-off of 450 eV was chosen for the plane wave expansion. The lattice parameters and ionic position were fully relaxed, and the total energy was converged within 10^{-5} eV per formula unit. The final forces on all ions are less than 0.02/Å.

Device fabrication

The $Cs_{0.1}FA_{0.6}MA_{0.3}Sn_{0.5}Pb_{0.5}I_3$ perovskite detectors have a device structure of ITO/PEDOT:PSS/perovskite/C_{60}/BCP/Ag. The PEDOT:PSS was spin-coated on the ITO substrates at 2000 rpm for 30 s and annealed at 100 °C for 10 min in the air. After cooling, the Sn-Pb perovskite films were spin-coated onto the substrates at 4000 rpm for 8 s in a nitrogen glovebox. The wet Sn-Pb perovskite films were immediately transferred into a vacuum chamber (120 mL) for a pumping time of 20 s at a vacuum degree of ~1 Pa. Then, the Sn-Pb perovskite films were annealed under a light radiation annealing for 1 min as we previously reported[61]. After cooling, the Sn-Pb perovskite films were post-treated by spinning a solution of $Sn(SCN)_2$ (0.5 mol mL^{-1}) in a 1:1 IPA:CB solvent at 4000 rpm for 30 s and annealed at 100 °C for 5 min. Then, the substrates were transferred to the evaporative chamber inside the nitrogen glovebox. C_{60} (15 nm)/BCP (7 nm)/Ag (150 nm) were sequentially deposited on the top of the perovskite by thermal evaporation.

Sn-Pb perovskite imager fabrication

The same Sn-Pb perovskite photodiodes were deposited directly on the pixel electrode array of the CMOS ROIC chip layer by layer. The hole transport layer, active layers and electron transport layers were prepared sequentially as described above, with the common pads covered by a tape. Then, a 200 nm ITO layer as a common top electrode was fabricated by magnetron sputtering in a DC mode at 100 W under an Ar atmosphere. Finally, the Sn-Pb perovskite imager was bonded to a metal casing in PGA format, providing a hermetic seal and electrical connection with the camera module.

Device characterizations

The XPS spectra for perovskite films were conducted using the AXIS SUPRA+ instrument from Shimadzu-Kratos (Japan). The perovskite film morphology was imaged with a scanning electron microscope (SEM, FEI Navo NanoSEM450). The AFM and KPFM images were obtained in the ambient atmosphere using a Bruker Dimension Icon XR AFM. The steady-state PL was measured using a laser confocal Raman spectrometer (LabRAM HR800, Horiba JobinYvon) and the light was illuminated from both the front and back surface of the perovskite films (excited by 532 nm). The TRPL was measured using a spectrofluorometer (QuantaMaster 8000 series fluorometers, Horiba), and the samples were excited by a 532 nm pulsed laser. The DLCP test used the Agilent E4294A impedance analyzer. The scanning voltage offset range is −0.1 V to 0.8 V and the a.c. voltage frequency was set to 10 kHz. The current density-voltage (*J-V*) and current density-time (*J-t*) curves were tested by an Agilent B1500A semiconductor characterization system. The 940 nm light sources were Thorlabs monochromatic light LEDs modulated by a pulse function generator (Agilent 332100 A). The noise current spectra were collected on a dynamic signal analyzer (Agilent 35670 A). The signal was amplified using a low-noise current preamplifier (Stanford Research Systems, SR570). The noise spectra were measured from 100 Hz to 100 kHz using a semicon-ductor parameter analyzer (Platform Design AutomationFS380) with a noise module. EQE measurements were performed in ambient air using a QE system (EnliTech) with monochromatic light focused on a device pixel and a chopper frequency of 20 Hz. The stability test in air were conducted at a relative humidity of 40% ± 10% both 25 °C and 65 °C. Electrical aging is carried out by using the KEITHLEY 2450 source meter in a nitrogen atmosphere of 25 °C, and then using the Agilent B1500A to test and record the aging data. All the devices were evaluated in their unencapsulated state. The images of the gray-scale were illuminated in 800 K blackbody radiation to ensure sufficiently strong and uniform light. The camera framing and focal length setting of the lens were under ISO test standards.

Acknowledgements

This work was financially supported by the National Key R&D Program of China (2023YFB3608900, 2024YFA1211200, 2021YFA0715502), Major Program (JD) of Hubei Province (2023BAA017), the National Natural Science Foundation of China (62174064, 52330004, U24A20510, 62204091, 62374068, 62304085, U22A2083), the Innovation Project of Optics Valley Laboratory (OVL2024ZD002, OVL2023ZD002), Supported by the Key Laboratory of Photoelectric Conversion and Utilization of Solar Energy (Innovation Fund Project SKLPCU24OP007), The University of New South Wales-Huazhong University of Science and Technology Strategic Partnership Research Seed Fund, Wuhan Science and Technology Innovation Bureau (2024010702020023), Guangdong Provincial Key Laboratory of Manufacturing Equipment Digitization (2023B1212060012), State Key Laboratory of Pulsed Power Laser Technology (SKL2023KF02), International Science and Technology Cooperation Project of Hubei Province (2024EHA027), the Exploration Project of Natural Science Foundation of Zhejiang Province (LY23F040005), the National Natural Science Foundation of Hubei Province (ZRMS2023002055), the Fund from Science, Technology and Innovation Commission of Shenzhen Municipality (GJHZ20220913143403007), the China Postdoctoral Science Foundation (2022M721243). The authors appreciate the Open and Shared Service Platform for Large Instruments and Equipment of School of Optical and Electronic Information of Huazhong University of Science and Technology (HUST) for offering SEM measurements. We thank the Optoelectronic Micro & Nano Fabrication and Characterizing Facility, Wuhan National Laboratory for Optoelectronics of Huazhong University of Science and Technology, and the Analytical and Testing Center of HUST for their support. The computation is completed in the HPC Platform of Huazhong University of Science and Technology. We thank the ROIC and imaging system support of Wenzhou InRight Technology Co., Limited.

Author details

[1]Wuhan National Laboratory for Optoelectronics (WNLO) and School of Optical and Electronic Information (SOEI), Huazhong University of Science and Technology, Wuhan, China. [2]State Key Laboratory of Pulsed Power Laser Technology, Hefei, China. [3]Optics Valley Laboratory, Wuhan, China. [4]Wenzhou Advanced Manufacturing Technology Research Institute of Huazhong University of Science and Technology, Wuhan, China. [5]JFS Laboratory, Wuhan, China. [6]Key Laboratory of Photoelectric Conversion and Utilization of Solar

Energy, Dalian Institute of Chemical Physics, Chinese Academy of Sciences, Dalian, China. [7]Shenzhen Huazhong University of Science and Technology Research Institute, Wuhan, China

Author contributions

C.G. and C.D. contributed equally to this work. C.G. wrote the manuscript. C.C., L.G. and J.T. conceived the concept, designed the experiments and revised the manuscript. C.G. and C.D. performed the most experimental studies. J.Z. and Y.Z. conducted the DFT theoretical calculations. Q.X. and B.J. helped to prepare the films and devices. L.C., Y.L. P.F. and B.S. participated in the discussion and data analysis. All authors read the manuscript and agree to its contents.

Data availability

The main data in this study are provided in the Supplementary Information. The data that support the findings of this study are available from the corresponding author upon reasonable request.

Conflict of interest

The authors declare no competing interests.

Supplementary information The online version contains supplementary material available at https://doi.org/10.1038/s41377-025-02127-y.

Received: 23 May 2025 Revised: 15 October 2025 Accepted: 7 November 2025

Published online: 20 January 2026

References

1. Chang, S. et al. Flexible and stretchable light-emitting diodes and photodetectors for human-centric optoelectronics. *Chem. Rev.* **124**, 768–859 (2024).
2. Meng, L., Xu, Q., Zhang, J. & Wang, X. Colloidal quantum dot materials for next-generation near-infrared optoelectronics. *Chem. Commun.* **60**, 1072–1088 (2024).
3. Ha, S. T. et al. Optoelectronic metadevices. *Science* **386**, eadm7442 (2024).
4. Abdullah, M. et al. Recent advancements in novel quantum 2D layered materials hybrid photodetectors from IR to THz: from principles to performance enhancement strategies. *Chem. Eng. J.* **504**, 158917 (2025).
5. Zhang, Y. et al. Reconstructive spectrometers: hardware miniaturization and computational reconstruction. *eLight* **5**, 23 (2025).
6. Saleem, M. I., Kyaw, A. K. K. & Hur, J. Infrared photodetectors: recent advances and challenges toward innovation for image sensing applications. *Adv. Opt. Mater.* **12**, 2401625 (2024).
7. Zou, T., Choi, T., Liu, A., Zhu, H. & Noh, Y.-Y. Printed quantum dot photodetectors for applications from the high-energy to the infrared region. *Nano Energy* **125**, 109539 (2024).
8. Wang, C., Zhang, X. & Hu, W. Organic photodiodes and phototransistors toward infrared detection: materials, devices, and applications. *Chem. Soc. Rev.* **49**, 653–670 (2020).
9. Morteza Najarian, A., Vafaie, M., Chen, B., García De Arquer, F. P. & Sargent, E. H. Photophysical properties of materials for high-speed photodetection. *Nat. Rev. Phys.* **6**, 219–230 (2024).
10. Saran, R. & Curry, R. J. Lead sulphide nanocrystal photodetector technologies. *Nat. Photonics* **10**, 81–92 (2016).
11. Nacpil, E. J. C., Han, J. & Jeon, I. Artificial intelligence-assisted robustness of optoelectronics for automated driving: a review. *IEEE Trans. Intell. Transp. Syst.* **25**, 57–73 (2024).
12. Li, Y. & Ibanez-Guzman, J. Lidar for autonomous driving: the principles, challenges, and trends for automotive lidar and perception systems. *IEEE Signal Process. Mag.* **37**, 50–61 (2020).
13. Liu, X., Lin, Y., Liao, Y., Wu, J. & Zheng, Y. Recent advances in organic near-infrared photodiodes. *J. Mater. Chem. C.* **6**, 3499–3513 (2018).
14. Yin, X. et al. PbS QD-based photodetectors: future-oriented near-infrared detection technology. *J. Mater. Chem. C.* **9**, 417–438 (2021).
15. Ba, K. & Wang, J. Advances in solution-processed quantum dots based hybrid structures for infrared photodetector. *Mater. Today* **58**, 119–134 (2022).
16. Wu, Q., Zhu, J. & Zhao, D. Progress and prospects for all-perovskite tandem solar cells. *J. Energy Chem.* **103**, 90–96 (2025).
17. Jiang, Q. & Zhu, K. Rapid advances enabling high-performance inverted perovskite solar cells. *Nat. Rev. Mater.* **9**, 399–419 (2024).
18. Yang, X. et al. Towards micro-PeLED displays. *Nat. Rev. Mater.* **8**, 341–353 (2023).
19. Han, T.-H. et al. A roadmap for the commercialization of perovskite light emitters. *Nat. Rev. Mater.* **7**, 757–777 (2022).
20. Sheng, Y., Wen, X., Jia, B. & Gan, Z. Direct laser writing on halide perovskites: from mechanisms to applications. *Light adv. manuf.* **4**, 14 (2024).
21. Du, S., Zhang, F. & Ma, L. Advances in femtosecond laser synthesis and micromachining of halide perovskites. *Light adv. manuf.* **5**, 41 (2024).
22. Sofia, A. et al. Enhancing the MA-free mixed halide perovskite efficiency and stability through bi-solvent engineering approach. *Light adv. manuf.* **6**, 10 (2025).
23. Dong, H. et al. Metal Halide Perovskite for next-generation optoelectronics: progresses and prospects. *eLight* **3**, 3 (2023).
24. Lee, S. J. et al. Lead halide perovskite sensitized WSe_2 photodiodes with ultrahigh open circuit voltages. *eLight* **3**, 8 (2023).
25. Wang, H. & Kim, D. H. Perovskite-based photodetectors: materials and devices. *Chem. Soc. Rev.* **46**, 5204–5236 (2017).
26. Wang, F. et al. Recent progress on electrical and optical manipulations of perovskite photodetectors. *Adv. Sci.* **8**, 2100569 (2021).
27. Miao, J. & Zhang, F. Recent progress on highly sensitive perovskite photodetectors. *J. Mater. Chem. C.* **7**, 1741–1791 (2019).
28. Ma, Y. et al. Day-Night imaging without infrared cutfilter removal based on metal-gradient perovskite single crystal photodetector. *Nat. Commun.* **15**, 7516 (2024).
29. Li, H. et al. Rational composition engineering for high-quality Pb–Sn photodetector toward sensitive near-infrared digital imaging arrays. *InfoMat* **7**, e12615 (2025).
30. Zhao, R. et al. Highly efficient and stable near-infrared photodetectors enabled from passivated tin–lead hybrid perovskites. *Nanotechnology* **34**, 215702 (2023).
31. Chang, Z. et al. High-Speed printing of narrow-band-gap Sn–Pb perovskite layers toward cost-effective manufacturing of optoelectronic devices. *ACS Appl. Mater. Interfaces* **15**, 32037–32046 (2023).
32. Lv, Y., Cen, G., Li, W., Zhao, C. & Mai, W. Highly sensitive fast-response near-infrared photodetectors based on triple cation Sn-Pb perovskite for pulse oximetry system. *Sci. China Mater.* **66**, 4704–4710 (2023).
33. Wang, Y. et al. Dual organic spacer cation quasi-2D Sn–Pb perovskite for solar cells and near-infrared photodetectors application. *Adv. Photonics Res.* **3**, 2200079 (2022).
34. Li, W. et al. The UV–vis-NIR broadband ultrafast flexible Sn-Pb perovskite photodetector for multispectral imaging to distinguish substance and foreign-body in biological tissues. *Adv. Opt. Mater.* **12**, 2301373 (2024).
35. Liu, F. et al. Highly efficient and stable self-powered mixed tin-lead perovskite photodetector used in remote wearable health monitoring technology. *Adv. Sci.* **10**, 2205879 (2023).
36. Chen, C. et al. Bioinspired, vertically stacked, and perovskite nanocrystal–enhanced CMOS imaging sensors for resolving UV spectral signatures. *Sci. Adv.* **9**, eadk3860 (2023).
37. Wang, X. et al. A monolithically integrated 640×512 CMOS-perovskite image sensor. in 2024 IEEE European Solid-State Electronics Research Conference (ESSERC) 213–216. https://doi.org/10.1109/ESSERC62670.2024.10719487. (IEEE, Bruges, Belgium, 2024).
38. Chen, Q. et al. All-inorganic perovskite nanocrystal scintillators. *Nature* **561**, 88–93 (2018).
39. He, Y. et al. Perovskite computed tomography imager and three-dimensional reconstruction. *Nat. Photonics* **18**, 1052–1058 (2024).
40. Ge, C. et al. Efficient Sn–Pb mixed perovskite solar cells via minimizing solvent oxidation. *Adv. Funct. Mater.* 2400075. https://doi.org/10.1002/adfm.202400075 (2024).
41. Lee, H., Kang, S. B., Lee, S., Zhu, K. & Kim, D. H. Progress and outlook of Sn–Pb mixed perovskite solar cells. *Nano Converg.* **10**, 27 (2023).
42. Liu, J. et al. Origins and suppression of Sn(II)/Sn(IV) oxidation in tin halide perovskite solar cells. *Adv. Energy Mater.* **13**, 2300696 (2023).
43. Chen, Q. et al. Unveiling roles of tin fluoride additives in high-efficiency low-bandgap mixed tin-lead perovskite solar cells. *Adv. Energy Mater.* **11**, 2101045 (2021).
44. Lin, R. Monolithic all-perovskite tandem solar cells with 24.8% efficiency exploiting comproportionation to suppress Sn(ii) oxidation in precursor ink. *Nat. Energy* **4**, 864–873 (2019).

45. Dai, Z. et al. Stable tin perovskite solar cells developed via additive engineering. *Sci. China Mater.* **64**, 2645–2654 (2021).
46. Liu, H. et al. Realizing high-detectivity near-infrared photodetectors in tin–lead perovskites by double-sided surface-preferred distribution of multifunctional tin thiocyanate additive. *ACS Energy Lett.* **8**, 577–589 (2023).
47. Wang, J. et al. Enhancing photostability of Sn-Pb perovskite solar cells by an alkylammonium pseudo-halogen additive. *Adv. Energy Mater.* **13**, 2204115 (2023).
48. Yu, Z. et al. Gradient doping in Sn–Pb perovskites by barium ions for efficient single-junction and tandem solar cells. *Adv. Mater.* **34**, 2110351 (2022).
49. Ollearo, R. et al. Ultralow dark current in near-infrared perovskite photodiodes by reducing charge injection and interfacial charge generation. *Nat. Commun.* **12**, 7277 (2021).
50. Li, H. et al. Low-dimensional inorganic tin perovskite solar cells prepared by templated growth. *Angew. Chem. Int. Ed.* **60**, 16330–16336 (2021).
51. Cong, H. et al. High-speed waveguide-integrated Ge/Si avalanche photodetector. *Chin. Phys. B* **25**, 058503 (2016).
52. Chow, W. W., Vawter, G. A. & Junpeng, G. Approaching intraband relaxation rates in the high-speed modulation of semiconductor lasers. *IEEE J. Quantum Electron.* **40**, 989–995 (2004).
53. Liu, J. et al. A near-infrared colloidal quantum dot imager with monolithically integrated readout circuitry. *Nat. Electron.* **5**, 443–451 (2022).
54. Rogalski, A., Antoszewski, J. & Faraone, L. Third-generation infrared photodetector arrays. *J. Appl. Phys.* **105**, 091101 (2009).
55. Kresse, G. & Furthmüller, J. Efficient iterative schemes for ab initio total-energy calculations using a plane-wave basis set. *Phys. Rev. B* **54**, 11169–11186 (1996).
56. Perdew, J. P., Burke, K. & Ernzerhof, M. Generalized gradient approximation made simple. *Phys. Rev. Lett.* **77**, 3865–3868 (1996).
57. Kresse, G. & Joubert, D. From ultrasoft pseudopotentials to the projector augmented-wave method. *Phys. Rev. B* **59**, 1758–1775 (1999).
58. Grimme, S., Antony, J., Ehrlich, S. & Krieg, H. A consistent and accurate ab initio parametrization of density functional dispersion correction (DFT-D) for the 94 elements H-Pu. *J. Chem. Phys.* **132**, 154104 (2010).
59. Grimme, S., Ehrlich, S. & Goerigk, L. Effect of the damping function in dispersion corrected density functional theory. *J. Comput. Chem.* **32**, 1456–1465 (2011).
60. Monkhorst, H. J. & Pack, J. D. Special points for Brillouin-zone integrations. *Phys. Rev. B* **13**, 5188–5192 (1976).
61. Ge, C. et al. Light radiation annealing enables unidirectional crystallization of vacuum-assisted Sn–Pb perovskites for efficient tandem solar cells. *Energy Environ. Sci.* **18**, 430–438 (2025).